Nano Research

Open Access

Research Article

Laser-engraved graphene architecture as an ultra-light freestanding lithium-free anode for lithium batteries

Jinze He[1], Lun Li[2,3] ✉, Rui Tan[4], Huazhang Zhang[3], Jie Wen[5], Mingxuan Wu[5], Chao Yin[5], Lai Tong[5], Lvping Fu[1], Biao Gao[1], Jinlong Yang[6] ✉, and Daping He[3] ✉

[1] *State Key Laboratory of Advanced Refractories, Wuhan University of Science and Technology, Wuhan 430081, China*
[2] *Hubei Longzhong Laboratory, Wuhan University of Technology Xiangyang Demonstration Zone, Xiangyang 441000, China*
[3] *Hubei Engineering Research Center of RF-Microwave Technology and Application, School of Physics and Mechanics, Wuhan University of Technology, Wuhan 430070, China*
[4] *Department of Chemical Engineering, Swansea University, Swansea SA1 8EN, UK*
[5] *School of Materials Science and Engineering, Wuhan University of Technology, Wuhan 430070, China*
[6] *Guangdong Provincial Key Laboratory of New Energy Materials Service Safety, College of Materials Science and Engineering, Shenzhen University, Shenzhen 518060, China*

Cite this article: *Nano Research*, **2026**, *19*, 94908611. https://doi.org/10.26599/NR.2026.94908611

ABSTRACT: Breakthroughs in high-capacity anodes represent a critical frontier in the development of next-generation high-specific-energy storage systems. However, the current high-capacity anodes of lithium batteries are confronted with numerous challenges, including uncontrolled volume expansion, lithium dendrite growth, dead lithium, and unstable solid electrolyte interphase (SEI) films. Herein, we firstly employ laser engraving technology to fabricate an ultra-light freestanding graphene film with through-hole array and defect-rich edges, which serves as a lithium-free anode that integrates lithium-ion intercalation and metallic lithium deposition. During discharge, the defect structures at the pore edges facilitate the adsorption of lithium ions and their rapid intercalation between graphene layers, forming the LiC_x framework. This enables the conversion of quasi-dead lithium through the solid-state pathway of Li → LiC_x → Li^+. Simultaneously, the vertically aligned through-holes homogenize ion flux and promote metallic lithium storage within the pores, thereby achieving high areal capacity, excellent reversibility, dendrite-free growth, and minimal volume change. As a result, this ultra-light freestanding lithium-free graphene anode (FLFGA) achieves highly reversible Li storage with 99.9% Coulombic efficiency (CE) over 1300 cycles and dendrite-free plating/stripping at a high areal capacity of 4 mAh·cm^{-2} (1350 mAh·g^{-1} anode). When paired with a high-loading $LiFePO_4$ (LFP) cathode (11.5 mg·cm^{-2}), the FLFGA||LFP full cell exhibits significantly enhanced cycling stability (500 cycles), outperforming most conventional Li metal battery, lean-Li battery, and anode-free Li battery systems. This work demonstrates a viable lithium-free anode strategy via laser-engraved graphene engineering, paving the way for durable, safe, and high-energy-density Li batteries.

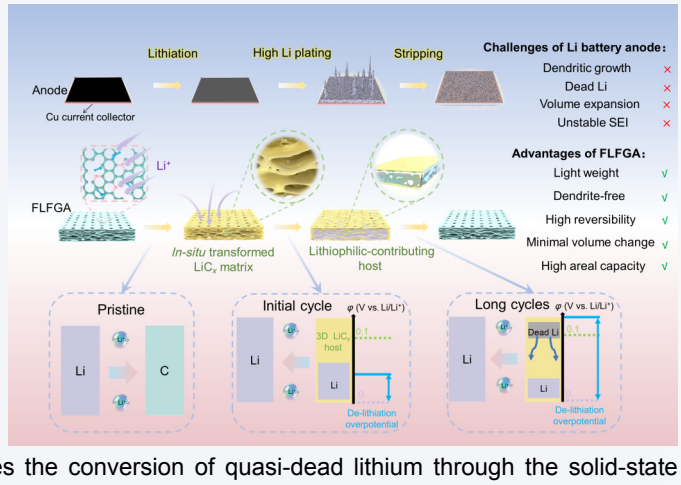

KEYWORDS: lithium battery, freestanding graphene film, lithium-free anode, laser engraving technology, dendrite-free

Received: January 26, 2026; **Revised:** February 22, 2026
Accepted: March 2, 2026

✉Address correspondence to Lun Li, lilunhy@whut.edu.cn; Jinlong Yang, yangjl18@szu.edu.cn; Daping He, hedaping@whut.edu.cn

1 Introduction

Currently, the commercial lithium-ion batteries predominantly employ graphite as the anode material, originally developed by Sony Corporation [1]. However, this configuration is increasingly inadequate to meet the demands of next-generation high-specific-energy storage systems required for new energy vehicles, low-

altitude aircraft, and artificial intelligence devices. To enhance battery energy density, the development of high-capacity anode materials has emerged as a critical research focus, including silicon anodes [2, 3], lithium metal anodes [4, 5], and anode-free configurations [6]. Lithium batteries based on these high-capacity anodes have progressively achieved energy densities exceeding 500 Wh·kg^{-1} [7]. Nevertheless, these novel high-capacity anodes often encounter challenges during cycling (Fig. 1(a)), such as uncontrolled volume expansion [8, 9], lithium dendrite growth [10], dead lithium formation [11], and unstable solid electrolyte interphase (SEI) layers [12], leading to low Coulombic efficiency (CE), rapid capacity degradation, and safety concerns.

To mitigate these issues, significant efforts have been devoted to optimizing electrolyte formulations [13], improving separator designs [14], and advancing current collector engineering [15]. In addition to these strategies, coatings with hybrid lithium storage mechanisms have shown considerable promise, wherein lithium-active materials, such as intercalation-type, alloy-type, or conversion-type, are introduced to *in-situ* form lithiophilic matrices, thereby regulating subsequent lithium deposition [16, 17]. Although these strategies have effectively improved the plating/stripping behavior of lithium metal, most of them involve modifying active materials on copper current collectors, where the metallic current collectors and additional coating layer account for a significant proportion of the battery weight. Recently, we have achieved large-scale production of lightweight, highly conductive, and thermally diffusive high-oriented dense graphene films (GF) to replace traditional metallic current collectors, which can enhance the energy density of lithium-ion batteries by 10%–20% while endowing the batteries with high safety and fast-charging capabilities [18–20]. Notably, when GFs are employed as anode current collectors, their surface/edge defects can induce localized lithium intercalation, demonstrating substantial potential for integrating intercalation-deposition reactions within a single graphene framework [19]. However, pristine GF featuring defect-free and densely stacked structure, exhibits poor redox activity at the superficial level, limiting its ability to suppress harmful Li formation. This highlights the urgent need to develop a redox-active GF that combines the intrinsic electronic conductivity and stable Li affinity, without relying on externally coated layers.

Herein, based on the previously developed graphene current collector [19], we fabricated an advanced freestanding lithium-free graphene anode (FLFGA) by laser etching technology (Fig. 1(b)), which can combine the intercalation of lithium ions and the deposition of metallic lithium to achieve high areal capacity, dendrite-free, and minimal volume expansion. The FLFGA fabricated via laser etching comprises a vertically aligned graphene array with through-holes, while simultaneously introducing a substantial quantity of heteroatoms and vacancy defects at the pore edges. During discharging, the FLFGA first undergoes Li intercalation to form a LiC_x framework, which subsequently enables the conversion of quasi-dead Li via the solid-state Li → LiC_x → Li^+ pathway (Fig. 1(c)). Additionally, the vertically aligned through-hole arrays can homogenize ion flux and decrease the local current density while accommodating volume changes by facilitating directional interlayer Li ions transport. As a result, the Li-ion storage is realized on this redox-active graphene substrate with a high CE of 99.9% over 1300 cycles, as well as a dendrite-free Li plating/stripping at high areal capacity of 4 mAh·cm^{-2}. Pairing with high areal loading $LiFePO_4$ (LFP) cathode (11.5 mg·cm^{-2}), the FLFGA||LFP full cell shows significantly improved cycling stability, withstanding 500 cycles with 45% capacity retention and maximized rate performance (97.2 mAh·g^{-1} at 5 C), which outperforms the majority of batteries assembled with anodes that are either lithium-free or lithium-poor. This study demonstrates a promising lithium-free anode strategy through laser-etched graphene engineering, enabling the design and realization of durable, safe, and high-energy-density lithium batteries.

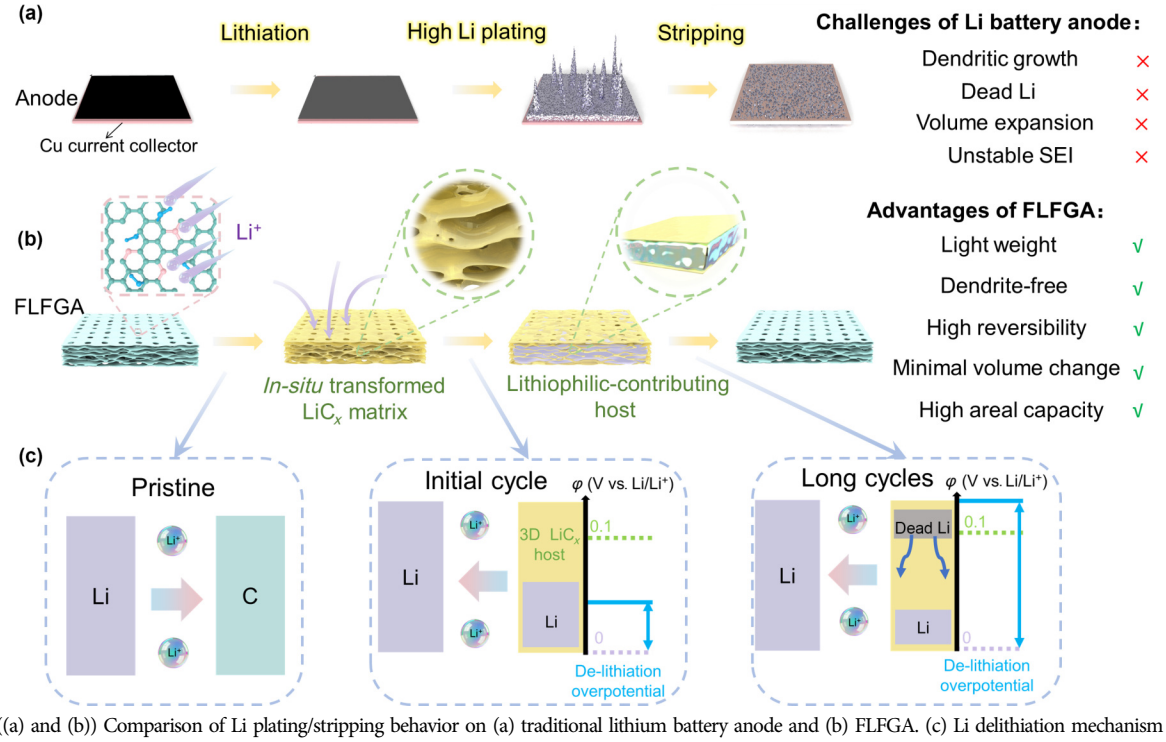

Figure 1 ((a) and (b)) Comparison of Li plating/stripping behavior on (a) traditional lithium battery anode and (b) FLFGA. (c) Li delithiation mechanism of FLFGA after initial cycle and long cycles.

2 Results and discussion

2.1 Fabrication and characterization of FLFGA

Pristine GF was first fabricated on a hundred-meter scale via a continuous coating–drying–carbonization–graphitization process according to our previous work [19].

Subsequently, vertically aligned through-hole array engineering design was implemented via a laser engraving process, yielding the intercalation-deposition integrated graphene anode with periodically distributed micropores (Fig. 2(a) and Fig. S1 in the Electronic Supplementary Material (ESM)). The resulting FLFGA contains uniform vertical channels with a pore diameter of 100 μm, a spacing of 100 μm (Fig. 2(b)), and other FLFGA samples with different inter-pore distances (200, 500, and 1000 μm, denoted as FLFGA-1, FLFGA-2, FLFGA-5, and FLFGA-10 in Fig. S2 in the ESM, unless otherwise specified, FLFGA hereafter refers to FLFGA-1), respectively, were prepared. The FLFGA exhibits the same thickness of 86 μm as pristine GF (Fig. 2(c) and Fig. S3 in the ESM), which featured a layered architecture of loosely stacked graphene sheets with abundant nano- to micron-scale interlayer pores, offering ample space for Li metal accommodation while mitigating volume changes. Mercury intrusion porosimetry further confirms that laser drilling enhances the overall pore accessibility of the graphene framework, as evidenced by the higher porosity and increased cumulative intrusion of FLFGA compared with pristine GF (Fig. S4 in the ESM). Moreover, the FLFGA shows a low area density of 2.96 mg·cm^{-2}, corresponding to significant reduction of 60%–85% and 12%–80% compared with previously reported Cu-based and GF-based anodes, respectively, for high-energy lithium batteries (Fig. 2(d)).

The robust and stable graphene skeleton also endows FLFGA with superior flexibility and durability. As shown in Fig. S5 in the ESM, FLFGA can withstand hundreds of repeated folding under 180° without any breakage or delamination. In contrast, Cu-based anodes fractured after merely 16 cycles and coated layer was almost completely detached from the GF surface after 5 cycles.

Raman spectra were collected to investigate the defective structure of FLFGA and GF (Fig. 2(e) and Fig. S6 in the ESM). The intensity ratio of the D-band to G-band (I_D/I_G), which is indicative of defect density, is 0.02 for pristine GF; this value is increased to 0.18 even for unperforated area in FLFGA. Moreover, I_D/I_G ratio increases along the direction close to the hole edge, and the maximum value can reach 0.7 in the laser-drilled boundaries, reflecting a defect-enriched area along the vertical channel. Pristine GF exhibits pronounced equatorial streak scattering with a narrow azimuthal intensity distribution, corresponding to a high Herman's orientation factor of 0.84 (Fig. S7(a) in the ESM). After laser treatment, FLFGA shows a broadened azimuthal distribution, reduced full width half maximum (FWHM), and a lower

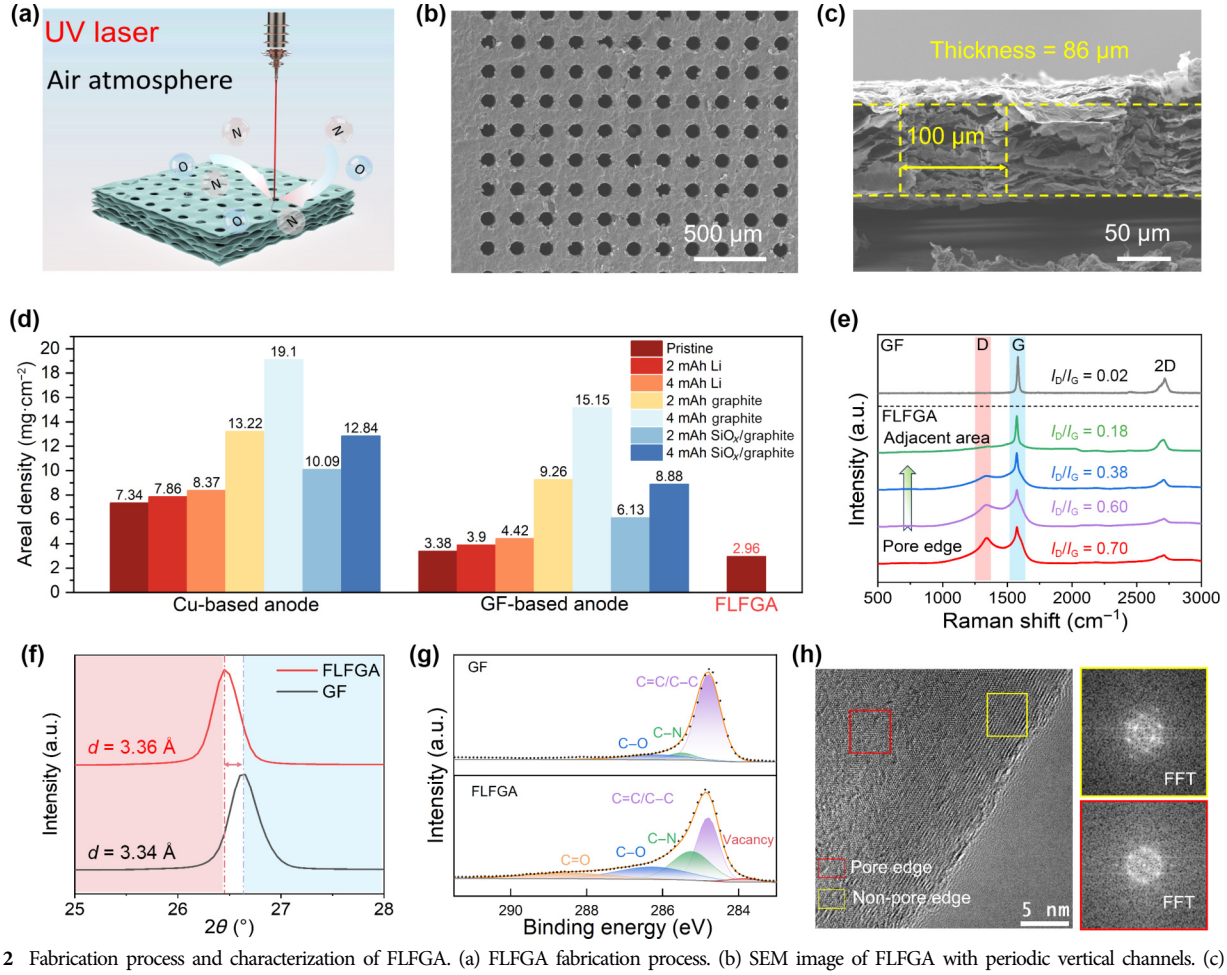

Figure 2 Fabrication process and characterization of FLFGA. (a) FLFGA fabrication process. (b) SEM image of FLFGA with periodic vertical channels. (c) Cross-sectional SEM image showing pore diameter. (d) Areal density comparison of FLFGA and anode. (e) Raman I_D/I_G ratio vs. distance from pore edge. (f) XRD patterns of GF and FLFGA. (g) C 1s XPS spectra of GF and FLFGA. (h) HR-TEM image with FFT images of pore edge lattice distortion.

orientation factor (f = 0.73) (Fig. S7(b) in the ESM), indicating a decrease in structural ordering and the reintroduction of defects into the graphene framework. X-ray diffraction (XRD) patterns (Fig. 2(f)) show that the (002) peak of GF appears at 26.6° with a standard interlayer spacing of 3.34 Å, while that of FLFGA shifts slightly to a lower angle, corresponding to an enlarged spacing of 3.36 Å. This increase in interlayer distance is possibly associated with the incorporation of heteroatoms at the edge of the holes during laser processing [21, 22].

X-ray photoelectron spectroscopy (XPS) was carried out to further clarify the defect types of FLFGA and GF (Fig. S8 in the ESM). The total content of C element is determined to be 82.2% for FLFGA, which is 13.0% lower than that of pristine GF, while O and N atoms are 4.4% and 13.4%, respectively, 11.3% and 3.4% higher than those of GF (Fig. S9 and Table S1 in the ESM). The increase of O and N elements is attributed to laser machining in ambient air, which causes oxidation of the carbon framework and reacts with atmospheric nitrogen to form C_xN_y [23]. C 1s spectra also confirm this defective structure. As depicted in Fig. 2(g), FLFGA exhibits stronger intensities of C=O (288.6 eV), C–O (286.5 eV), and C–N (285.6 eV) peaks, which represent noticeably increased chemical bond abundance compared with that in GF [24]. More importantly, a pronounced peak at 283.7 eV, corresponding to vacancy-type defects, was detected in FLFGA but absent in GF, evidencing the generation of vacancy-type defects-enriched structure during the formation of ordered microchannels by laser engraving [25]. High-resolution transmission electron microscopy (HR-TEM) analysis, with corresponding fast Fourier transform (FFT) patterns, revealed the structural difference between the pore-edge ablation region and the non-pore region of FLFGA (Fig. 2(h)). The HR-TEM image of the non-pore region displayed ordered lattice fringes, verifying its highly crystalline structure. The corresponding FFT showed a hexagonal reciprocal-space pattern, indicative of a sp^2-hybridized graphitic structure. In contrast, the pore-edge region exhibited distorted and disordered lattice domains in the HR-TEM image, together with a diffuse halo in the FFT, which is characteristic of a defective structure [26]. Based on the morphology and spectroscopic analysis, FLFGA can be characterized as a carbon matrix with grafted heteroatom and vacancy structure at the edge of the holes. These chemical and structural defect-enriched properties enhance the electrochemical reactivity of the graphene architecture.

2.2 Validation of defect engineering-driven Li-ions storage

Density functional theory (DFT) calculations were first employed to elucidate the function mechanism of introduced defects on lithiation behavior. Pristine graphene model shows a low Li adsorption energy of −1.44 eV, indicating a poor lithiation capability [18]. While the adsorption energy is increased to −1.69 eV when introduced with vacancy defects, −2.72 eV with N/O heteroatom defects, and −3.55 eV with both (Fig. 3(a)). These results demonstrate that laser-induced vacancies and heteroatom defects act synergistically to enhance electrochemical activity and promote the formation of a stable LiC_x framework during initial lithiation. To verify the effect of introduced defects under real condition, optical and scanning electron microscopy (SEM) images of three electrodes were recorded after galvanostatic discharging to 0 V. The color and morphology of Cu and GF hardly change, while FLFGA changes from gray to golden yellow, and the nanosheets in FLFGA obviously thicken upon lithiation, suggesting the successful formation of a lithiated LiC_x framework throughout the porous matrix (Fig. S10 in the ESM). Corresponding lithiation products are also detected by XRD patterns (Fig. 3(b)). GF shows only weak LiC_{12} and LiC_{24} peaks, in contrast, FLFGA exhibits focused LiC_x peaks on LiC and LiC_{12}, and LiC_{24} accompanied by weak LiC_6, suggesting deeper lithiation for FLFGA prior to Li metal deposition [27–29]. Unlike inert GF substrates, the defective graphene architecture facilitates high Li-ions storage ability, which can undergo *in-situ* transformation into a lithiated scaffold, serving as a lithiophilic intermediate to regulate subsequent Li deposition [30–32].

In-situ Raman testing during galvanostatic cycling provides dynamic insights into the lithiation/plating and stripping/delithiation process (Fig. 3(c)). At open-circuit potential, the D band (~ 1350 cm^{-1}) remains prominent while the G band (~ 1580 cm^{-1}) is suppressed, consistent with partial Li intercalation. During discharge (~ 1300 s), both bands gradually shift to higher wavenumbers, indicating progressive interlayer insertion of Li^+. After 1300 s, the Raman signal vanishes, marking the onset of metallic Li deposition. During charging (3300–4000 s), the D, G, and 2D (2700 cm^{-1}) bands reappear, demonstrating reversible Li stripping and partial restoration of the graphene lattice. These results indicate that FLFGA acts as a hybrid anode, ensuring highly reversible lithiation/delithiation and guiding subsequent Li plating and stripping [33].

XPS depth profiling reveals distinct SEI composition on the FLFGA and pristine GF after discharge (0 V). For FLFGA, the C 1s spectra show persistent Li–C (~ 283.9 eV), C–N (~ 285.7 eV), C–O (~ 286.5 eV), and C=O (~ 288.6 eV) peaks after 60 and 120 s etching, indicating homogeneously distributed LiC_x structures (Fig. 3(d)). In contrast, GF exhibits extremely weak Li–C signals on the upper surface and this signal disappears rapidly as etching depth increases, suggesting surface-confined lithiation and limited internal utilization (Fig. 3(e)). Li 1s spectra further confirm this contrast. In FLFGA (Fig. 3(f)), LiF (~ 56.8 eV), Li_2CO_3 (~ 55.4 eV), and $ROCO_2Li$ (where R represents an alkyl group, ~ 54.2 eV) signals remain stable at all depths, indicative of a deeply embedded, uniform SEI. By contrast, GF (Fig. 3(g)) shows significant attenuation of SEI-related signals after shallow etching, implying poor SEI coverage and interfacial instability [12, 34, 35]. These results indicate that the uniform SEI and self-converted, lithiophilic LiC_x framework in FLFGA can ensure interfacial stability and facilitate highly reversible Li intercalation.

In addition, voltage profiles of Li inserting-plating storage show that FLFGA achieves a Li intercalation capacity of ~ 0.5 $mAh{\cdot}cm^{-2}$ until the voltage drops to 0 V vs. Li/Li^+ (Fig. 3(h)). Long-term insertion and extraction tests demonstrate an exceptional cycling performance under this capacity, as evidenced by the high CE of 99.9% over 1300 cycles (Fig. 3(i)) and highly overlapped discharge–charge profiles. This high reversibility is superior to GF and other samples (Fig. S11 in the ESM), confirming the excellent Li^+ storage capability of FLFGA [36].

2.3 Uniform Li deposition within FLFGA

To verify the enhanced Li plating/stripping behavior guided by the activated graphene architecture, asymmetric cells were assembled to reveal the morphology evolution of deposited Li on Cu, GF, and various FLFGA substrates. For Cu and GF, the discharging voltage straightly drops below 0 V vs. Li/Li^+ owing to the electrochemical inert property. Regarding FLFGA, with increasing defect density,

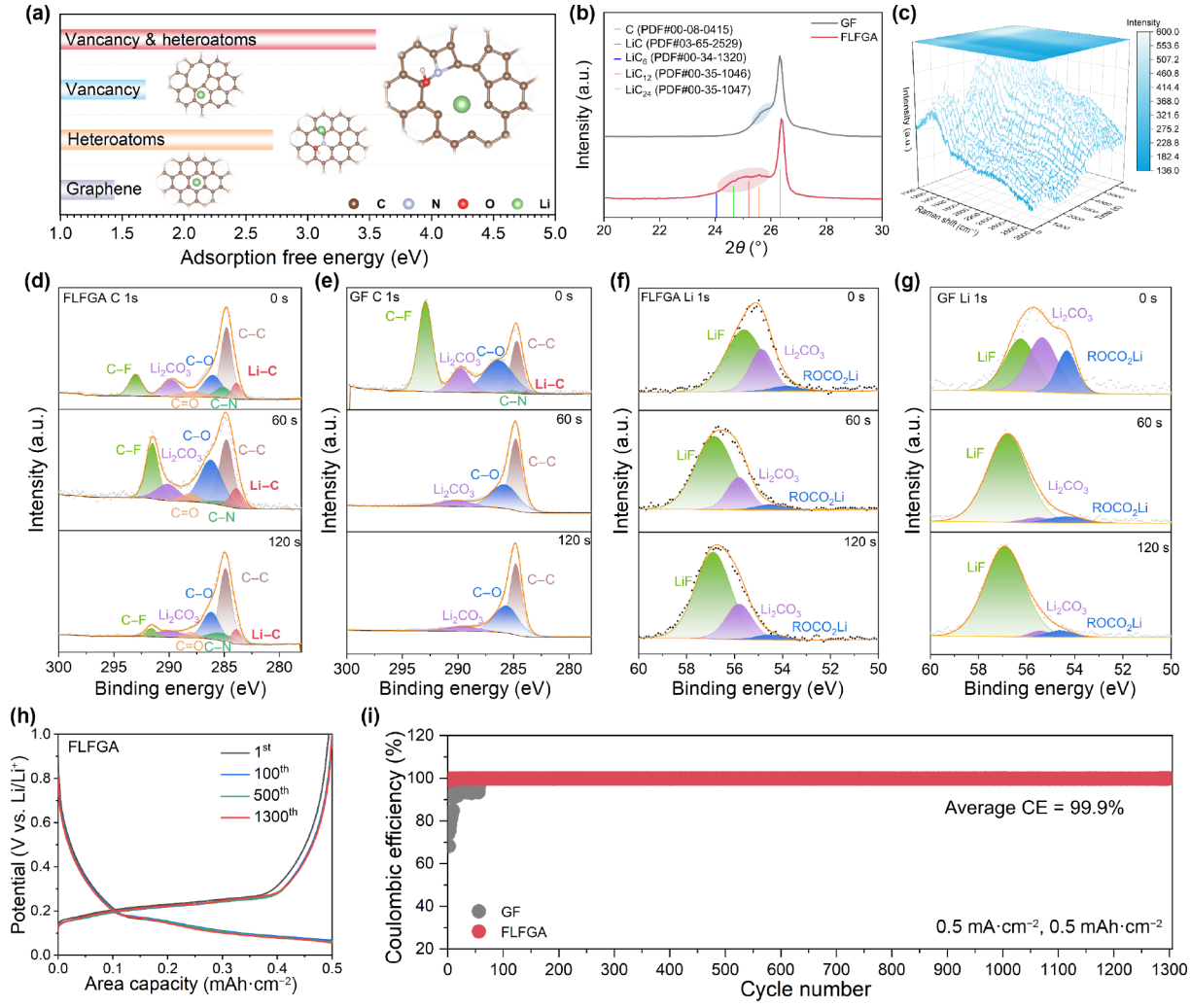

Figure 3 *In-situ* self-transformation of FLFGA to LiC_x. (a) DFT calculation results, Li adsorption energies on different graphene substrates. (b) XRD patterns of GF and FLFGA. (c) *In-situ* Raman spectra during one cycle. ((d)–(g)) XPS C 1s and Li 1s spectra of ((d) and (f)) FLFGA and ((e) and (g)) GF after lithiation. (h) Voltage–capacity profiles and (i) CE of GF and FLFGA electrodes tested in half-cells at 0.5 mA·cm^{-2} and 0.5 mAh·cm^{-2}.

the redox activity also becomes higher, accompanied by a smaller energy barrier for Li nucleation (Fig. 4(a)). In detail, Cu and GF exhibit much higher nucleation overpotentials of 84.3 and 51.1 mV than that of FLFGA electrodes, particularly with FLFGA-1 exhibiting the lowest value of 4.6 mV (Fig. 4(b)). The reduced overpotential demonstrates the effectiveness of our laser-engraved graphene architecture in regulating homogeneous Li nucleation.

Electrochemical impedance spectroscopy (EIS) measurements (Fig. 4(c)) reveal that FLFGA exhibits the lowest interfacial resistance (~ 40 Ω), outperforming GF (~ 100 Ω) and Cu (~ 200 Ω). After 50 cycles, FLFGA shows further impedance reduction to ~ 17 Ω due to electrode activation and stable SEI formation, while GF remains at ~ 55 Ω (Fig. S12 in the ESM). The persistently higher impedance of GF and Cu highlights their poor interfacial conductivity and unstable Li deposition behavior. FLFGA, by contrast, provides enhanced ionic conductivity and interfacial stability through its porous, functionalized structure [37].

Li deposition morphologies at different capacities are compared in Figs. 4(d)–4(o). After initial activation (0.1 mA·cm^{-2}, 0.1 mAh·cm^{-2}), Cu surface exhibits many protrusions (Fig. 4(d)), quickly develops into uneven Li lumps at 1 mAh·cm^{-2} (Fig. 4(e)), and extensive dendritic growth at 4 mAh·cm^{-2} (Fig. 4(f)). Cross-sectional SEM reveals substantial volume expansion and protruding dendrites (Fig. 4(g)), showing severe safety concerns. A large number of micro-cracks appeared on GF after activation (Fig. 4(h)), which can be attributed to localized lithiation-induced stress [38]. Li deposition on GF at 1 mAh·cm^{-2} shows uneven Li clusters (Fig. 4(i)), while at 4 mAh·cm^{-2} it leads to significant surface accumulation accompanied by dendrite formation (Fig. 4(j)). Cross-sections show Li confined to the surface, with limited internal penetration (Fig. 4(k)), reflecting poor structural utilization due to the dense morphology. In stark contrast, FLFGA maintains a smooth and intact surface after activation (Fig. 4(l)). At 1 mAh·cm^{-2}, Li nucleation directionally occurred around pore interiors (Fig. 4(m)), with FLFGA-1 exhibiting the most uniform deposition behavior (Fig. S13 in the ESM). Even deposited with 4 mAh·cm^{-2}, over 60% of the FLFGA pores remain unfilled (Fig. 4(n)), and the deposited Li layer on the surface remains smooth and compact (Fig. S14 in the ESM). Corresponding to the extremely high lithium storage capacity (1350 mAh·g_{anode}^{-1}) and the absence of dendrite growth. Cross-sectional SEM images show that the membrane thickness increases only from 83 to 90 μm after deposition, corresponding to a volume expansion of approximately 5%. This minimal expansion confirms interlayer-dominated Li deposition, preferentially starting from the bottom and guided by

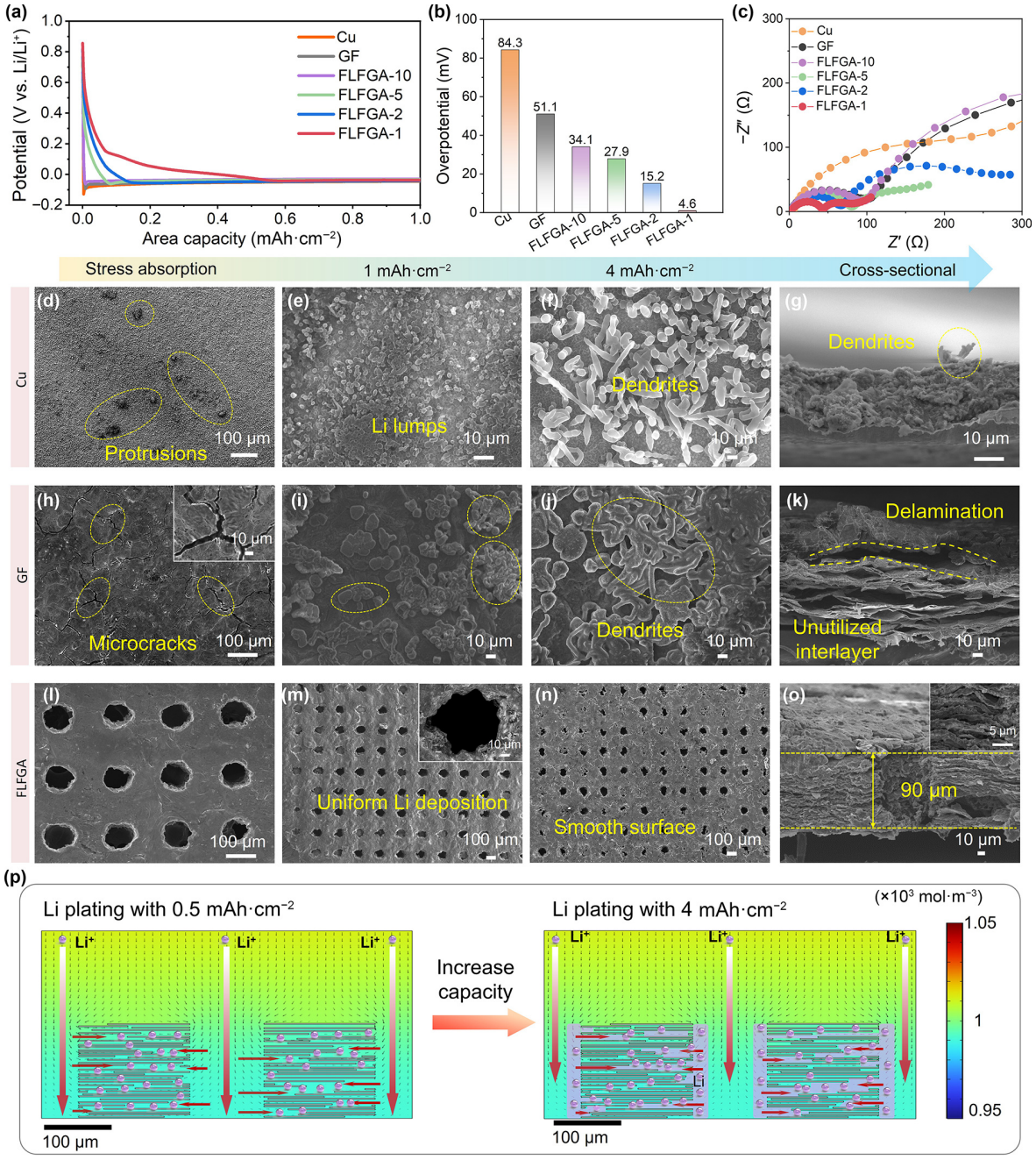

Figure 4 Dendrite-free Li deposition. (a) Voltage–capacity profiles for initial Li deposition on FLFGA variants. (b) Comparison of nucleation overpotentials for Cu, GF, and FLFGA electrodes. (c) First-cycle EIS spectra of Cu, GF, and FLFGA electrodes. ((d)–(o)) SEM images of lithium deposition morphologies on ((d)–(g)) Cu, ((h)–(k)) GF, and ((l)–(o)) FLFGA electrodes at different deposition capacities. (p) Finite-element simulated Li-ion concentration profiles of FLFGA.

vertically aligned channels within the FLFGA matrix (Fig. 4(o)), overcoming kinetic limitations of two-dimensional graphene interfaces.

Operando optical microscopy also reveals intrinsically different Li storage mechanisms on FLFGA and GF under identical plating conditions (4 mA·cm^{-2}). As shown in Fig. S15(a) in the ESM, FLFGA undergoes a hybrid lithium storage process, where Li^+ ions are first intercalated into the defect-rich graphene framework to form a LiC_x host, followed by regulated metallic Li deposition with a uniform and compact surface morphology, whereas GF exhibits a surface-dominated Li plating accompanied by mossy and dendritic growth (Figs. S15(b) and S15(c) in the ESM).

The superior structure of FLFGA is further confirmed by simulations. Finite-element modelling reveals distinct transport behaviors between GF and FLFGA. Ion concentration profiles show that in pristine GF, Li^+ accumulates at the surface while the interior remains ion-deficient, indicating limited vertical penetration (Fig. S16 in the ESM). By contrast, FLFGA maintains a much more homogeneous Li^+ distribution, enabled by vertically aligned perforations that facilitate direct ionic access to internal layers and reduce transport tortuosity. At high deposition capacities, Li preferentially fills the internal pores and subsequently extends along the perforation edges, leading to dense and uniform Li deposition. Current density simulations further demonstrate that GF suffers

from pronounced field localization and current crowding (Fig. 4(p)), which accelerates dendrite growth (Fig. S17(a) in the ESM), whereas FLFGA exhibits uniform current distribution throughout the framework (Fig. S17(b) in the ESM). These results explain the enhanced intercalation, LiC_x scaffold formation, and dendrite suppression observed experimentally, consistent with the long-term stability of FLFGA [39].

Structural control over Li behavior was further validated by comparing FLFGA with a densely stacked counterpart (Dense-FLFGA) featuring same porosity. As shown in Fig. S18 in the ESM, aggressive dendrite growth clusters mainly appeared on the surface around the pores, highlighting the importance of interlayer voids architecture for directed ion transport [40]. Beyond interlayer accessibility, the role of defect engineering was further clarified by comparing laser-drilled GFs with physically drilled GFs (PDGF). Raman analysis confirms that PDGF exhibits a nearly undetectable D band, and the I_D/I_G ratio is 0.02 which remains consistent with that of pristine GF (Fig. S19 in the ESM), indicating that physical perforation alone can not induce defective structure. Consequently, after Li deposition at 4 mAh·cm^{-2}, PDGF shows pronounced surface-localized Li accumulation and mossy/dendritic growth (Fig. S20 in the ESM), indicating that vertically aligned channels without defect activation are ineffective in regulating uniform Li nucleation and growth, further confirming the unique advantages of the FLFGA. Upon subsequent stripping, FLFGA shows an almost residue-free, smooth surface, whereas GF retains dead Li deposits (Fig. S21 in the ESM), highlighting that the defect-rich, channel-guided framework of FLFGA enables more complete Li recovery, while the inert GF surface exhibits irreversible Li accumulation. Collectively, these comparisons demonstrate that the vertically aligned pores in FLFGA promote efficient ion transport and internal Li accommodation, suppress dendrite formation, and ensure structural stability, enabling highly reversible Li plating and stripping, where the periodic defect-engineered channels guide Li ions to deposit directionally within the interlayers of the films, highlighting the advantages of FLFGA.

2.4 Cycling stability of FLFGA

To further evaluate the reversibility and practicality of Li plating/stripping behaviors, various types of asymmetrical cells with different FLFGA were assembled. Figure 5(a) shows the cycling performance of Li||FLFGA half-cells under 1 mA·cm^{-2}/1 mAh·cm^{-2}. FLFGA-1 manifests the most stable CE of ~ 99.1% over 300 cycles. In contrast, GF, Cu, and other FLFGA with different pore spacing exhibit obvious CE fluctuations or pronounced CE decays. Superior capacity stability is also observed for FLFGA in Fig. 5(b), whereas GF displays evident capacity decay beyond 100 cycles (Fig. S22(a) in the ESM), reflecting unstable plating/stripping behavior. As the deposition capacity increases to 2 mAh·cm^{-2} (Fig. 5(c) and Fig. S22(b) in the ESM), FLFGA retains a high CE of ~ 98.4% for more than 100 cycles, while the CE of GF rapidly deteriorates and fails within 50 cycles. Upon further increasing the plated capacity to 4 mAh·cm^{-2}, the CE of FLFGA can still be held at 98% even after 65 cycles (Fig. S22(c) in the ESM).

Typical voltage profiles of FLFGA during cycling (Fig. 5(d) and Fig. S21(d) in the ESM) reveal a two-stage reaction process. At 1 mA·cm^{-2}, Li^+ is first intercalated into the graphene host (where Q denotes the areal capacity, $Q_{intercalating}$ = 0.49 mAh·cm^{-2}),

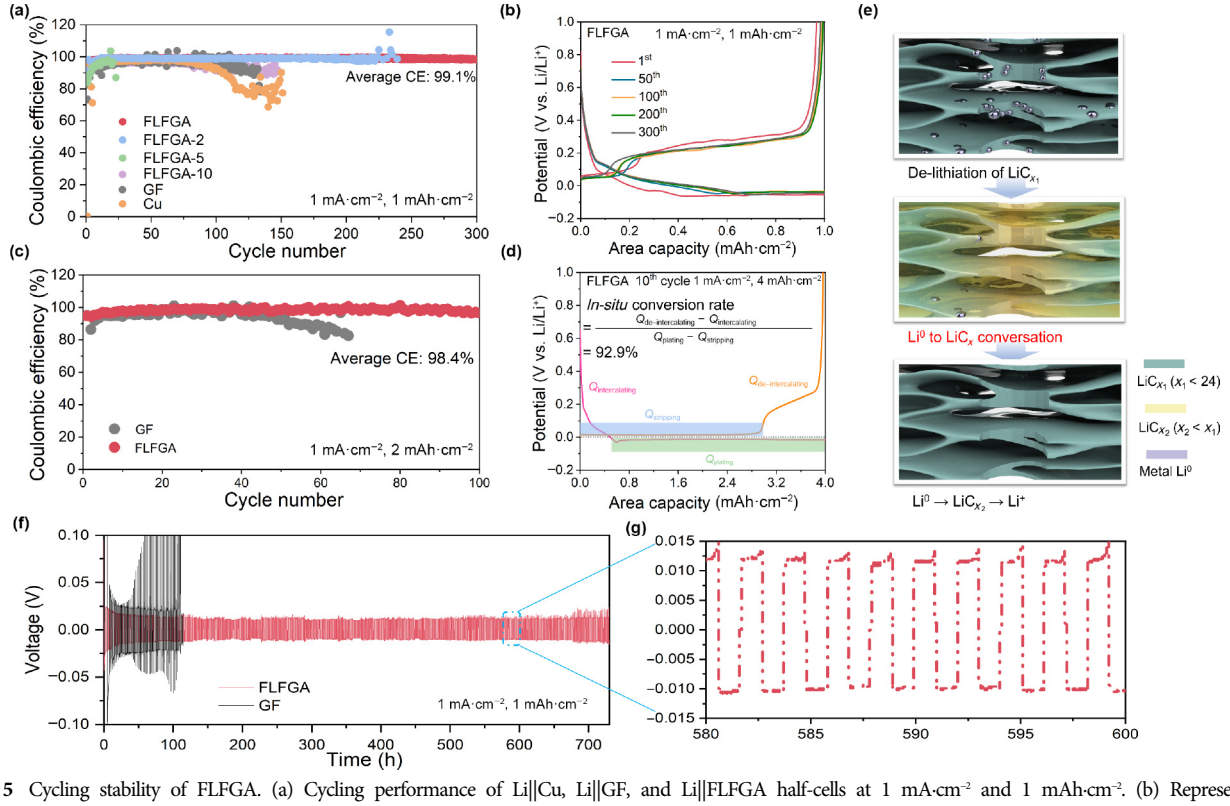

Figure 5 Cycling stability of FLFGA. (a) Cycling performance of Li||Cu, Li||GF, and Li||FLFGA half-cells at 1 mA·cm^{-2} and 1 mAh·cm^{-2}. (b) Representative voltage–capacity profiles of FLFGA during cycling. (c) CE of GF and FLFGA electrodes in half-cells at 1 mA·cm^{-2} and 2 mAh·cm^{-2}. (d) Typical voltage–capacity curves illustrating lithium intercalation and plating stages at 1 mA·cm^{-2}/4 mAh·cm^{-2}. (e) Schematic of *in-situ* conversion of quasi-dead lithium to LiC_x, mitigating dead lithium accumulation. (f) Long-term cycling of symmetric cells with FLFGA and GF electrodes. (g) Overpotential evolution and polarization stability of FLFGA during extended cycling.

forming a LiC_x scaffold, followed by metallic Li plating ($Q_{plating}$ = 3.51 mAh·cm^{-2}). Upon delithiation, 2.95 mAh·cm^{-2} of Li is stripped ($Q_{stripping}$), leaving residual Li on the electrode. Interestingly, a subsequent de-intercalation process delivers 1.01 mAh·cm^{-2} ($Q_{de\text{-}intercalating}$), more than double the initial intercalation capacity. This suggests that residual Li is reactivated via a solid-state Li → LiC_x → Li^+ conversion pathway. The *in-situ* conversion rate (CR), calculated as ($Q_{de\text{-}intercalating}$ − $Q_{intercalating}$)/($Q_{plating}$ − $Q_{stripping}$), reaches ~ 92.9%, confirming high Li recovery efficiency and reversibility driven by the intercalation-plating synergy. The LiC_x framework plays a dual role: guiding Li plating/stripping and enabling solid-state reaction with pseudo-dead Li through chemical potential coupling (Fig. 5(e)) [41]. The FLFGA scaffold is thereby transformed into a self-converting active host, which facilitates uniform Li accommodation and preserves interfacial stability over prolonged cycling.

Symmetric cell cycling results (Fig. 5(f)) further demonstrate the superior stability of FLFGA. While GF and Cu cells short-circuit after ~ 100 and ~ 60 h, FLFGA sustains a low, stable overpotential (~ 20 mV) for over 730 h without voltage spikes. The enlarged view between 580–600 h (Fig. 5(g)) highlights its exceptional polarization stability. Figure S23 benchmarks FLFGA against conventional Li metal battery (LMB), lean-Li battery (LLMB), and anode-free Li battery (AFLMB) systems. FLFGA demonstrates the lowest nucleation overpotential and the highest cycling reversibility among all tested systems, establishing it as a superior Li-free anode for high-energy Li batteries.

2.5 Performance of full pouch cell with FLFGA

To demonstrate the practical potential of FLFGA in flexible electronic devices, pouch cell using high-loading LFP cathode and FLFGA was assembled (Fig. 6(a)). Noted that the large-area FLFGA can be easily scaled up, as demonstrated by an effective area of 50 cm × 30 cm (Fig. 6(b)), which is suitable for the use of industrial lithium batteries manufacturing. Even under repeated 180° bending, the full-charged cells stably powered 55 series-connected 3 V light-emitting diode (LED) bulbs for approximately 40 min (Video S1 in the ESM) without any brightless attenuation (Fig. 6(c)). After 50 cycles of harsh bending, the full cell remained fully operational, demonstrating the practicality and durability of our designed FLFGA in full cells. Figure 6(d) shows typical plateaus of 3.4–3.5 and 0.1–0.2 V vs. Li/Li^+ for LFP cathode and our engineered FLFGA, respectively. Accordingly, the FLFGA||LFP full

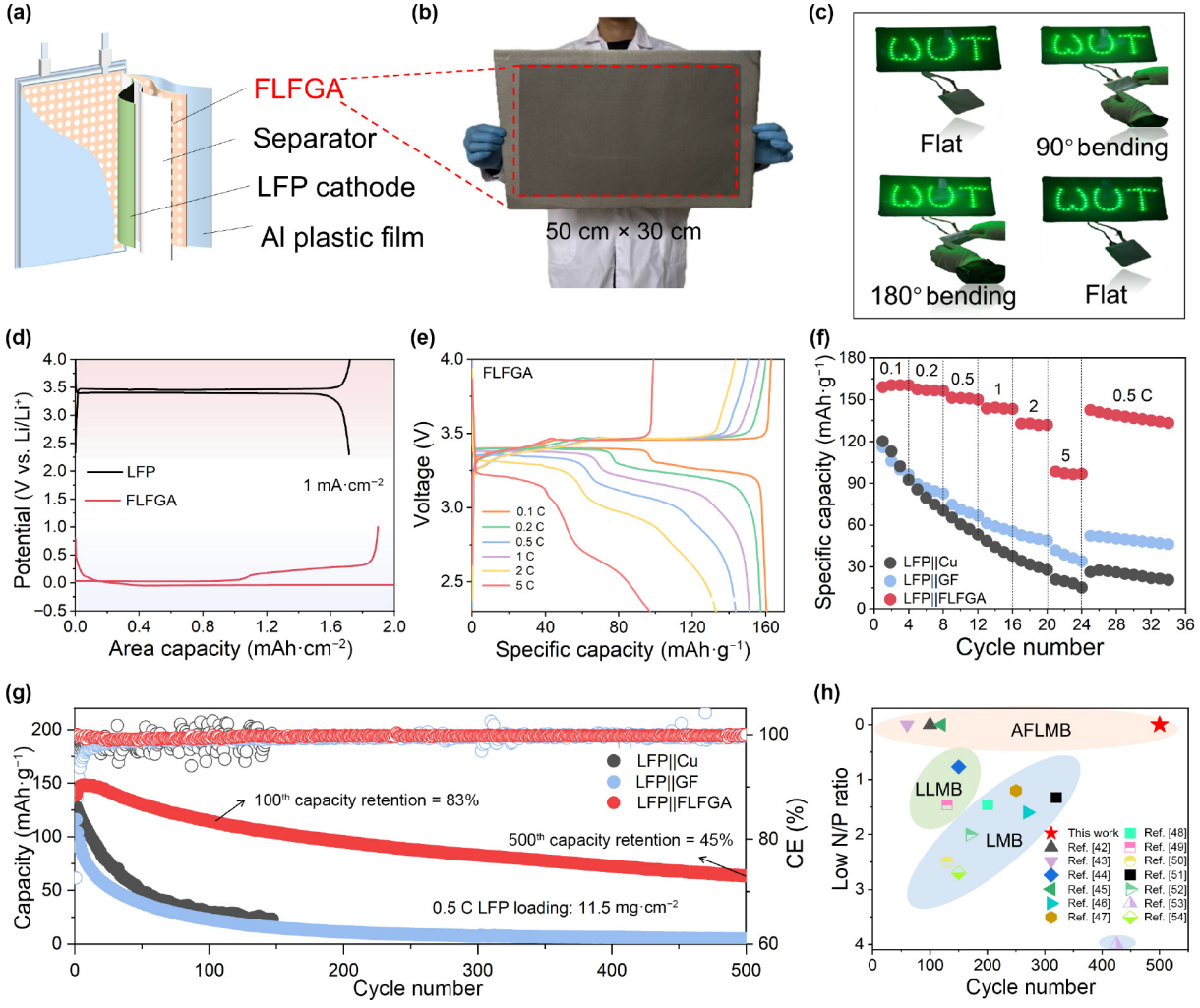

Figure 6 Assembly and performance of full pouch cells. (a) Schematic of an FLFGA-based pouch cell. (b) Large-scale optical image of FLFGA. (c) Cycling stability of the pouch cell and operation of 55 LEDs under repeated 180° bending. (d) Discharge–charge profiles within the potential windows of −0.1–1 and 2.3–4.0 V at 1 mA·cm^{-2}. (e) Voltage–capacity curves of rate test from 0.1 to 5 C. (f) Rate capability of Cu, GF, and FLFGA from 0.1 to 5 C. (g) Cycling performance of full cells with Cu, GF, and FLFGA. (h) Comparison of N/P ratios and cycle life among FLFGA-based battery, AFLMB, LLMB, and LMB.

cell exhibits a stable operating voltage of ~ 3.3 V (Fig. 6(e)), slightly lower than that of theoretical LFP||Li plateau due to the intrinsic lithiation potential of FLFGA partially offsetting the cathode potential. Rate performance (Fig. 6(f)) further validates the advantages of FLFGA. Highly reversible capacities are maintained from 0.1 to 5 C, with 93.6 mAh·g^{-1} retained at high rate of 5 C, far exceeding full cells assembled with GF (~ 42.0 mAh·g^{-1}) and Cu (~ 18.5 mAh·g^{-1}) (Figs. S24 and S25 in the ESM). This high-rate stability is attributed to the vertical porous architecture and the LiC_x framework, which collectively facilitate efficient ion diffusion and uniform Li deposition within the FLFGA. After fast charging/discharging at 5 C, (Fig. S26 in the ESM) the FLFGA still maintains an intact structure without any visible dead Li, showing distinct ability to inhibit dendrite growth. As a result, cathode structure can also remain well preserved after cycling (Fig. S27 in the ESM).

Full cells with FLFGA also demonstrate obviously better cycling stability than those with pristine GF and Cu anodes (Fig. 6(g)). Voltage–capacity curves at 0.5 C (Fig. S28 in the ESM) show that FLFGA exhibits a stable voltage plateau with a low polarization. FLFGA-based full cells deliver an initial capacity of 139 mAh·g^{-1}, ~ 83% and ~ 45% of which is respectively maintained after 100 and 500 cycles. Comparatively, the capacities of LFP||GF and LFP||Cu heavily decay to 5 mAh·g^{-1} (Fig. S29 in the ESM) and 23 mAh·g^{-1} (Fig. S30 in the ESM), respectively, which are only 4% and 18% of their initial capacities. Moreover, full cells with FLFGA display a highly stable CE of 99.9% during long-term cycling, while serious CE fluctuation occurred for other two full cells.

Figure 6(h) compares the cycling life and N/P ratio based on the Li metal battery, lean-Li battery, and our FLFGA-based battery systems [42–54], among which FLFGA-based pouch cell delivers the longest cycle life with the lowest N/P ratio, confirming the architecture superiority of FLFGA as a high-performance and practically feasible anode for high-energy and long-life lithium batteries.

3 Conclusions

In summary, we proposed a laser-engineered FLFGA that enables lightweight and stable cycling for high-energy cell. This design leverages controlled defect densities to modulate redox activity for self-converting into LiC_x scaffold, thereby mitigating Li nucleation overpotential and suppressing dendrite formation. At the defect-enriched edge of the hole array, a uniform and stable SEI was formed, contributing to a densely packed Li morphology. The vertically aligned channels resulting from defect engineering facilitate Li transport into graphene interlayers, which provides more space for Li deposition, effectively restricting volume expansion. FLFGA exhibits a high CE of 99.9% over 1300 cycles for Li-ion storage, and ultra-low volume expansion of ~ 5% even at a Li deposition capacity of 4 mAh·cm^{-2}. Li-free full cells achieve prominent cycling stability operated for 500 cycles. This work verifies the effectiveness of our activated graphene architecture by laser engraving technology, shedding light on the development of future durable, safe, and high-energy-density Li batteries.

Electronic Supplementary Material: Supplementary material (experimental section, additional Figs. S1–S24, Table S1, and Video S1) is available in the online version of this article at https://doi.org/10.26599/NR.2026.94908611.

Data availability

All data needed to support the conclusions in the paper are presented in the manuscript and the Electronic Supplementary Material. Additional data related to this paper may be requested from the corresponding author upon request.

Acknowledgements

We sincerely acknowledge financial support from the National Natural Science Foundation of China (Nos. 22279097 and 52172217), the first batch of joint funding by the China Postdoctoral Science Foundation and Hubei Province (No. 2025T015HB), the 76th Batch of General Funding of the China Postdoctoral Science Foundation (No. 2024M762511), Natural Science Foundation of Hubei Province (No. 2025AFB038), Guangdong Basic and Applied Basic Research Foundation (No. 2024B1515020031), and Postdoctoral Independent Innovation Fund (No. 104972025RSCbs0171).

Declaration of competing interest

All the contributing authors report no conflict of interests in this work.

Author contribution statement

J. Z. H. and L. L. conceived and designed the research. J. L. Y. and J. Z. H. performed data curation, analysis, and took the lead in writing and revising the manuscript. L. L. assisted in funding acquisition and manuscript preparation. R. T., J. L. Y., and D. P. H. contributed to conceptualization and methodology. H. Z. Z. and C. Y. conducted simulations and assisted in data analysis. J. W., M. X. W., and L. T. assisted in the experiments. L. P. F. and B. G. contributed to visualization. J. L. Y. and D. P. H. supervised the project. All authors discussed the results and commented on the manuscript. All the authors have approved the final manuscript.

Use of AI statement

None.

References

[1] Yoshino, A. The birth of the lithium-ion battery. *Angew. Chem., Int. Ed.* **2012**, *51*, 5798–5800.

[2] An, W. L.; Gao, B.; Mei, S. X.; Xiang, B.; Fu, J. J.; Wang, L.; Zhang, Q. B.; Chu, P. K.; Huo, K. F. Scalable synthesis of ant-nest-like bulk porous silicon for high-performance lithium-ion battery anodes. *Nat. Commun.* **2019**, *10*, 1447.

[3] Sun, L.; Liu, Y. X.; Shao, R.; Wu, J.; Jiang, R. Y.; Jin, Z. Recent progress and future perspective on practical silicon anode-based lithium ion batteries. *Energy Storage Mater.* **2022**, *46*, 482–502.

[4] Lin, D. C.; Liu, Y. Y.; Liang, Z.; Lee, H. W.; Sun, J.; Wang, H. T.; Yan, K.; Xie, J.; Cui, Y. Layered reduced graphene oxide with nanoscale interlayer gaps as a stable host for lithium metal anodes. *Nat. Nanotechnol.* **2016**, *11*, 626–632.

[5] He, X.; Zhang, K.; Zhu, Z. Q.; Tong, Z. F.; Liang, X. 3D-hosted lithium metal anodes. *Chem. Soc. Rev.* **2024**, *53*, 9–24.

[6] Jo, C. H.; Sohn, K. S.; Myung, S. T. Feasible approaches for anode-free lithium-metal batteries as next generation energy storage systems. *Energy Storage Mater.* **2023**, *57*, 471–496.

[7] Liu, J.; Bao, Z. N.; Cui, Y.; Dufek, E. J.; Goodenough, J. B.; Khalifah,

P.; Li, Q. Y.; Liaw, B. Y.; Liu, P.; Manthiram, A. et al. Pathways for practical high-energy long-cycling lithium metal batteries. *Nat. Energy* **2019**, *4*, 180–186.

[8] Lin, D. C.; Liu, Y. Y.; Cui, Y. Reviving the lithium metal anode for high-energy batteries. *Nat. Nanotechnol.* **2017**, *12*, 194–206.

[9] Luo, C.; Hu, H.; Zhang, T.; Wen, S. J.; Wang, R.; An, Y.; Chi, S. S.; Wang, J.; Wang, C. Y.; Chang, J. et al. Roll-to-roll fabrication of zero-volume-expansion lithium-composite anodes to realize high-energy-density flexible and stable lithium-metal batteries. *Adv. Mater.* **2022**, *34*, 2205677.

[10] Zhao, F.; Zhang, J. H.; Chen, J. X.; Gu, Z. Y.; Fan, X. Z.; Zhu, L.; Na, H. L.; Dong, M. X.; Guan, C.; Kong, L. Lithium salt association-mediated interfacial charge exchange for low-temperature lithium-metal batteries: Beyond lithium de-solvation manner. *Research* **2025**, *8*, 0802.

[11] Liu, H.; Ji, Y. C.; Li, Y.; Zheng, S. S.; Dong, Z. H.; Yang, K.; Cao, A. M.; Huang, Y. X.; Wang, Y. C.; Shen, H. F. et al. Regulating lithium affinity of hosts for reversible lithium metal batteries. *Interdiscip. Mater.* **2024**, *3*, 297–305.

[12] Li, L.; Ji, P. X.; Huang, M.; Zhang, Z. X.; Wang, H.; Verpoort, F.; Yang, J. L.; He, D. P. Hybrid ionic/electronic interphase enabling uniform nucleation and fast diffusion kinetics for stable lithium metal anode. *Chin. Chem. Lett.* **2024**, *35*, 109144.

[13] Ma, M. Y.; Huang, R. Z.; Ling, M.; Hu, Y. S.; Pan, H. L. Towards stable electrode–electrolyte interphases: Regulating solvation structures in electrolytes for rechargeable batteries. *Interdiscip. Mater.* **2023**, *2*, 833–854.

[14] Liu, Z. F.; Hu, Q. M.; Guo, S. T.; Yu, L.; Hu, X. L. Thermoregulating separators based on phase-change materials for safe lithium-ion batteries. *Adv. Mater.* **2021**, *33*, 2008088.

[15] Zhou, B. X.; Bonakdarpour, A.; Stoševski, I.; Fang, B. Z.; Wilkinson, D. P. Modification of Cu current collectors for lithium metal batteries—A review. *Prog. Mater. Sci.* **2022**, *130*, 100996.

[16] Yang, Z. W.; Chen, T.; Chen, D. Q.; Shi, X. Y.; Yang, S.; Zhong, Y. J.; Liu, Y. X.; Wang, G. K.; Zhong, B. H.; Song, Y. et al. A Ge/carbon atomic-scale hybrid anode material: A micro-nano gradient porous structure with high cycling stability. *Angew. Chem., Int. Ed.* **2021**, *60*, 12539–12546.

[17] Liu, Y. M.; Qin, X. Y.; Liu, F.; Huang, B. H.; Zhang, S. Q.; Kang, F. Y.; Li, B. H. Basal nanosuit of graphite for high-energy hybrid Li batteries. *ACS Nano* **2020**, *14*, 1837–1845.

[18] Zhao, Y. W.; Yang, J. L.; Ma, J. J.; Wu, Q.; Qian, W.; Wang, Z.; Zhang, H. N.; He, D. P.; Mu, S. C. Highly reduced graphene assembly film as current collector for lithium ion batteries. *ACS Sustain. Chem. Eng.* **2021**, *9*, 8635–8641.

[19] Li, L.; Yang, J. L.; Tan, R.; Shu, W.; Low, C. J.; Zhang, Z. X.; Zhao, Y.; Li, C.; Zhang, Y. J.; Li, X. C. et al. Large-scale current collectors for regulating heat transfer and enhancing battery safety. *Nat. Chem. Eng.* **2024**, *1*, 542–551.

[20] Tang, Z. Z.; Chen, J.; Zhu, D.; Sheng, L.; Yang, Y.; Yang, K.; Wang, J. L.; Tang, Y. P.; He, X. M.; Xu, H. A large-area uniform three-dimensional covalent organic framework membrane for stabilizing Li-metal electrodes via solvation cages. *Research* **2025**, *8*, 0926.

[21] Chen, P. F.; Yang, X. R.; Chang, Y. F.; Qian, W.; Fu, H. Q.; Xu, W. X.; Ren, L.; Wang, Z.; Zu, H. R.; Wang, D. S. et al. Superior microwave shielding modulation based on rapidly prepared graphene metasurface. *Natl. Sci. Rev.* **2025**, *12*, nwaf395.

[22] Hu, X.; Ma, Y. T.; Qu, W. J.; Qian, J.; Li, Y. T.; Chen, Y.; Zhou, A. B.; Wang, H. R.; Zhang, F. L.; Hu, Z. Q. et al. Large interlayer distance and heteroatom-doping of graphite provide new insights into the dual-ion storage mechanism in dual-carbon batteries. *Angew. Chem., Int. Ed.* **2023**, *62*, e202307083.

[23] Shen, Q. L.; Wang, T. Y.; Song, Q.; Ye, F.; Li, H. J.; Fu, M. W. Unraveling of the laser drilling of carbon/carbon composites: Ablation mechanisms, shape evolution, and damage evaluation. *Int. J. Mach. Tools Manuf.* **2023**, *184*, 103978.

[24] Liu, Z. Y.; Li, Q. W.; Song, Q. M.; Li, J.; Xu, Z. M. Mechanochemical upcycling of spent battery graphite into a self-cleaning adsorbent for wastewater treatments. *Research* **2025**, *8*, 1015.

[25] Kwon, H.; Lee, J. H.; Roh, Y.; Baek, J.; Shin, D. J.; Yoon, J. K.; Ha, H. J.; Kim, J. Y.; Kim, H. T. An electron-deficient carbon current collector for anode-free Li-metal batteries. *Nat. Commun.* **2021**, *12*, 5537.

[26] Pender, J. P.; Jha, G.; Youn, D. H.; Ziegler, J. M.; Andoni, I.; Choi, E. J.; Heller, A.; Dunn, B. S.; Weiss, P. S.; Penner, R. M. et al. Electrode degradation in lithium-ion batteries. *ACS Nano* **2020**, *14*, 1243–1295.

[27] Iyo, A.; Ogino, H.; Ishida, S.; Eisaki, H. Dramatically accelerated formation of graphite intercalation compounds catalyzed by sodium. *Adv. Mater.* **2023**, *35*, 2209964.

[28] Sun, Y. M.; Zheng, G. Y.; Seh, Z. W.; Liu, N.; Wang, S.; Sun, J.; Lee, H. R.; Cui, Y. Graphite-encapsulated Li-metal hybrid anodes for high-capacity Li batteries. *Chem* **2016**, *1*, 287–297.

[29] Drüe, M.; Seyring, M.; Rettenmayr, M. Phase formation and microstructure in lithium-carbon intercalation compounds during lithium uptake and release. *J. Power Sources* **2017**, *353*, 58–66.

[30] Duan, J.; Zheng, Y. H.; Luo, W.; Wu, W. Y.; Wang, T. R.; Xie, Y.; Li, S.; Li, J.; Huang, Y. H. Is graphite lithiophobic or lithiophilic? *Natl. Sci. Rev.* **2020**, *7*, 1208–1217.

[31] Xue, Z. Q.; Wang, Z. Y.; Zhang, J. D.; Lu, Y.; Huang, W. Z.; Chen, A. B.; Zhao, C. Z.; Elena, K.; Elena, K.; Vladimir, K. et al. The role, formation and characterization of LiC_6 in composite lithium anodes. *New Carbon Mater.* **2023**, *38*, 641–655.

[32] Sun, X.; Liu, H.; Ren, K. F.; Tang, W. B.; Guo, C.; Bao, W. Z.; Yu, F.; Cheng, X. B.; Li, J. F. Understanding the coupling mechanism of intercalation and conversion hybrid storage in lithium-graphite anode. *Small* **2024**, *20*, 2401675.

[33] Sole, C.; Drewett, N. E.; Hardwick, L. J. *In-situ* Raman study of lithium-ion intercalation into microcrystalline graphite. *Faraday Discuss.* **2014**, *172*, 223–237.

[34] Li, L.; Fu, H. Q.; Yang, J. L.; Wang, P. Y.; Zhang, H. Z.; Zhao, X.; Xiao, Z. T.; Liu, Z. H.; Kou, Z. K.; Wang, Z. B. et al. A dual-confined lithium nucleation and growth design enables dendrite-free lithium metal batteries. *J. Mater. Chem. A* **2022**, *10*, 11659–11666.

[35] Cui, C. Y.; Yang, C. Y.; Eidson, N.; Chen, J.; Han, F. D.; Chen, L.; Luo, C.; Wang, P. F.; Fan, X. L.; Wang, C. S. A highly reversible, dendrite-free lithium metal anode enabled by a lithium-fluoride-enriched interphase. *Adv. Mater.* **2020**, *32*, 1906427.

[36] Shi, P.; Hou, L. P.; Jin, C. B.; Xiao, Y.; Yao, Y. X.; Xie, J.; Li, B. Q.; Zhang, X. Q.; Zhang, Q. A successive conversion-deintercalation delithiation mechanism for practical composite lithium anodes. *J. Am. Chem. Soc.* **2022**, *144*, 212–218.

[37] Koo, D.; Kwon, B.; Lee, J.; Lee, K. T. Asymmetric behaviour of Li/Li symmetric cells for Li metal batteries. *Chem. Commun.* **2019**, *55*, 9637–9640.

[38] Neale, A. R.; Milan, D. C.; Braga, F.; Sazanovich, I. V.; Hardwick, L. J. Lithium insertion into graphitic carbon observed via *operando* Kerr-gated Raman spectroscopy enables high state of charge diagnostics. *ACS Energy Lett.* **2022**, *7*, 2611–2618.

[39] Wang, S. H.; Yin, Y. X.; Zuo, T. T.; Dong, W.; Li, J. Y.; Shi, J. L.; Zhang, C. H.; Li, N. W.; Li, C. J.; Guo, Y. G. Stable Li metal anodes via regulating lithium plating/stripping in vertically aligned microchannels. *Adv. Mater.* **2017**, *29*, 1703729.

[40] Ni, S. Y.; Sheng, J. Z.; Zhang, C.; Wu, X.; Yang, C.; Pei, S. F.; Gao, R. H.; Liu, W.; Qiu, L.; Zhou, G. M. Dendrite-free lithium deposition and stripping regulated by aligned microchannels for stable lithium metal batteries. *Adv. Funct. Mater.* **2022**, *32*, 2200682.

[41] Chen, Z. D.; Luo, Y. T.; Yang, D. S.; Hu, Y. H.; Hou, H. R.; Koratkar,

N.; Zhou, G. M.; Liu, W. Intraparticle alloying-plating reaction for high-performing lithium metal batteries with low volume expansion. *Mater. Today* **2025**, *86*, 74–86.

[42] Assegie, A. A.; Chung, C. C.; Tsai, M. C.; Su, W. N.; Chen, C. W.; Hwang, B. J. Multilayer-graphene-stabilized lithium deposition for anode-free lithium-metal batteries. *Nanoscale* **2019**, *11*, 2710–2720.

[43] Wondimkun, Z. T.; Tegegne, W. A.; Jiang, S. K.; Huang, C. J.; Sahalie, N. A.; Weret, M. A.; Hsu, J. Y.; Hsieh, P. L.; Huang, Y. S.; Wu, S. H. et al. Highly-lithiophilic Ag@PDA-GO film to suppress dendrite formation on Cu substrate in anode-free lithium metal batteries. *Energy Storage Mater.* **2021**, *35*, 334–344.

[44] Gong, M. J.; Yu, R. H.; Zhou, C.; Yu, Y. K.; Pan, Q. M.; Dong, C. X.; Shen, C. L.; Guan, Y. J.; Sun, C. L.; Mai, L. Q. et al. Mechanically robust current collector with gradient lithiophilicity induced by spontaneous lithium ion diffusion for stable lean-lithium metal batteries. *ACS Nano* **2024**, *18*, 20648–20658.

[45] Ouyang, Z. F.; Wang, S.; Wang, Y.; Muqaddas, S.; Geng, S. T.; Yao, Z. B.; Zhang, X.; Yuan, B.; Zhao, X. J.; Xu, Q. C. et al. An ultralight composite current collector enabling high-energy-density and high-rate anode-free lithium metal battery. *Adv. Mater.* **2024**, *36*, 2407648.

[46] Du, J. M.; Wang, W. Y.; Wan, M. T.; Wang, X. C.; Li, G. C.; Tan, Y. C.; Li, C. H.; Tu, S. B.; Sun, Y. M. Doctor-blade casting fabrication of ultrathin Li metal electrode for high-energy-density batteries. *Adv. Energy Mater.* **2021**, *11*, 2102259.

[47] Zhang, J. M.; Zhou, Y.; Tu, F. Y.; Ma, Y.; Zhang, H. Z.; Song, D. W.; Shi, X. X.; Zhang, L. Q. *In-situ* constructing lithiophilic and ion/electron dual-regulated current collector for highly stable lithium metal batteries. *Chem. Eng. J.* **2022**, *428*, 132510.

[48] Chen, H.; Yang, Y. F.; Boyle, D. T.; Jeong, Y. K.; Xu, R.; De Vasconcelos, L. S.; Huang, Z. J.; Wang, H. S.; Wang, H. X.; Huang, W. X. et al. Free-standing ultrathin lithium metal-graphene oxide host foils with controllable thickness for lithium batteries. *Nat. Energy* **2021**, *6*, 790–798.

[49] Li, C.; Li, Y.; Yu, Y. K.; Shen, C. L.; Zhou, C.; Dong, C. X.; Zhao, T. H.; Xu, X. One-pot preparation of lithium compensation layer, lithiophilic layer, and artificial solid electrolyte interphase for lean-lithium metal anode. *ACS Appl. Mater. Interfaces* **2022**, *14*, 19437–19447.

[50] Zhang, K.; Liu, W.; Gao, Y. L.; Wang, X. W.; Chen, Z. X.; Ning, R. Q.; Yu, W.; Li, R. L.; Li, L.; Li, X. et al. A high-performance lithium metal battery with ion-selective nanofluidic transport in a conjugated microporous polymer protective layer. *Adv. Mater.* **2021**, *33*, 2006323.

[51] Chu, X.; Dong, F. L.; Jiang, Y.; Qiao, Q. M.; Xie, H. M. Synergetic regulation of bulk reconstruction and preferential orientation realizing long-lifespan thin Li anodes for high-energy-density lithium metal batteries. *J. Energy Chem.* **2025**, *105*, 418–426.

[52] Kim, S.; Cho, K. Y.; Kwon, J.; Sim, K.; Eom, K.; Fuller, T. F. *In-situ* electrochemical interfacial manipulation enabling lithiophilic Li metal anode with inorganic-rich solid electrolyte interphases for stable Li metal batteries. *Small Struct.* **2024**, *5*, 2400254.

[53] Li, Z. D.; Huai, L. Y.; Li, S.; Ma, M. M.; Luo, K. L.; Zhao, Y.; Wang, D. Y.; Sun, X. L.; Peng, Z. Insight into bulk charge transfer of lithium metal anodes by synergism of nickel seeding and LiF–Li_3N–Li_2S Co-doped interphase. *Energy Storage Mater.* **2021**, *37*, 491–500.

[54] Zhang, C.; Fan, H. M.; Chen, X. L.; Xu, H.; Lou, J. T.; Li, Y.; Huang, Y. H.; Li, S. Non-sticky Li-alloy leaves for long-lasting secondary batteries. *Energy Environ. Sci.* **2022**, *15*, 5251–5260.